Clays Clay Miner., Vol. 70, No. 1:1–19, 2022
https://doi.org/10.1007/s42860-022-00176-7

ORIGINAL PAPER

Extraction of ^{40}Ar-^{39}Ar ages from a multicomponent mixture: a case study from the Tatra Mountains, Poland

Artur Kuligiewicz · Michał Skiba · Marek Szczerba · Chris M. Hall · Dorota Bakowska

Accepted: 19 February 2022

Abstract Extraction of meaningful information on the timing of fault activity from clay gouges using radiometric dating methods, such as those based on the K-Ar system, can be challenging. One of the factors complicating interpretation of the radiometric dating results is the presence of multiple K-bearing components in the gouge material. In the current study, an attempt was made to develop a new interpretative method for K-Ar and ^{40}Ar-^{39}Ar dating, capable of handling a three-component mixture. In addition, the mineral composition of clay gouges from the Tatra Mountains (Poland), which has not been investigated before, is reported. The mineral compositions of the bulk clay gouge material and separated size fractions were determined by X-ray diffractometry and Fourier-transform infrared spectroscopy. The gouge samples were composed of quartz, dioctahedral mica (as a discrete phase and as a component of mixed-layered illite-smectite), and chlorite, commonly with plagioclase and more rarely with K-feldspar, dioctahedral smectite, calcite, anatase, or trace kaolinite. One feldspar-free sample containing three mica polytypes ($1M_d$, $1M$, and $2M_1$) was chosen for dating with the ^{40}Ar-^{39}Ar method. The results of ^{40}Ar-^{39}Ar dating were interpreted using three concepts: Illite Age Analysis (IAA), a method based on the *MODELAGE* software, and a newly developed three-component concept. The age values obtained with IAA were −14 Ma ± 31 Ma and 180 ± 91 Ma for authigenic ($1M_d$) and inherited ($1M + 2M_1$) components, respectively. The *MODELAGE*-based approach returned –4 ± 40 Ma and 165 ± 62 Ma. The three-component approach returned age values of polytypes as follows: $1M_d$, 15 ± 37 Ma; $1M$, 135 ± 57 Ma; $2M_1$, 121 ± 56 Ma based on the medians and the interquartile ranges of non-normal distributions of Monte Carlo-simulated age values. The results obtained indicated that the $1M_d$ polytype was probably formed during the most recent stage of fault activity, while $1M$ and $2M_1$ polytypes are of equal age, roughly.

Keywords ^{40}Ar-^{39}Ar dating · Clay gouges · Illite · Mica · Polytype quantification · Shear zones · Tatra Mountains

This article was updated to correct errors in the formatting of Equations 5, 6, 7, and 8 that were introduced during the production process.

A. Kuligiewicz (✉) · M. Szczerba · D. Bakowska
Institute of Geological Sciences, Polish Academy of Sciences, Senacka 1, 31-002 Kraków, Poland
e-mail: ndkuligi@cyf-kr.edu.pl

M. Skiba
Institute of Geological Sciences, Jagiellonian University, Gronostajowa 3a, 30-387 Kraków, Poland

C. M. Hall
Department of Earth and Environmental Sciences, University of Michigan, Ann Arbor, MI 48109-1005, USA

Introduction

Clay gouges or fault gouges are non-cohesive fault rocks containing <30% of visible fragments (Brodie et al., 2004; Sibson, 1977). One of the most important goals of recent studies of clay gouges has been to constrain the timing of the studied faulting (e.g. Abad et al., 2017;

Boles et al., 2018; Fitz-Díaz et al., 2016; Haines & van der Pluijm, 2012; Mancktelow et al., 2016; Viola et al., 2013). Clay gouges usually contain significant amounts of K-bearing micas; therefore, K-Ar and ^{40}Ar-^{39}Ar dating have been used widely for studies of these rocks. The ^{40}Ar-^{39}Ar method has gained more attention because it eliminates potential errors caused by measuring K and Ar content from two different portions of a sample, which is a standard procedure in K-Ar dating (Clauer, 2013; Clauer et al., 2012). As pointed out by Dong et al. (1995, 1997), fine-grained materials such as clay minerals require vacuum encapsulation before ^{40}Ar-^{39}Ar dating in order to account for Ar loss due to the recoil effect from crystals with sizes of a few nanometers.

Fault gouges commonly contain both minerals inherited from the parent material and authigenic minerals, i.e. those formed during, or shortly after, tectonic deformation (Haines & van der Pluijm, 2008; Solum et al., 2005; Torgersen et al., 2014; van der Pluijm et al., 2001; Ylagan et al., 2002). In such a case, age values obtained during isotopic dating represent mixtures of two or more constituents. In addition, for shear zones with a history of multiple reactivation episodes, the final composition may not be a mixture of just two end members. Each reactivation event may potentially have led to creation of a distinct mineral population and may or may not have reset the K-Ar system within previously crystallized authigenic components (Bense et al., 2014).

Various methods have been proposed to extract the end-member ages from the age values of mixtures (Dong et al., 2000; Grathoff & Moore, 1996; Pevear, 1992; Szczerba & Środoń, 2009; Ylagan et al., 2000). In most of the proposed methods, the material was assumed to be a mixture of two components, i.e. non-authigenic and authigenic, that could be distinguished mineralogically, e.g. by polytype quantification. The high-temperature $2M_1$ dioctahedral mica ("illite") polytype was assumed to have been inherited, while low-temperature $1M$ and $1M_d$ polytypes of dioctahedral mica were believed to be authigenic. A common practice in the field is, however, to use only $1M_d$ and $2M_1$ polytypes for description of fault gouge material (van der Plujm & Hall, 2015), because the $1M$ polytype is rare and requires specific formation conditions (Peacor et al., 2002). In addition, the $1M$ polytype is believed not to occur during normal prograde diagenesis of pelitic rocks (Peacor et al., 2002), and many of the studies on fault dating were of clay gouges hosted in sedimentary rocks (e.g. Solum et al., 2005). On the other hand, the $1M$ polytype was demonstrated to co-exist with the $2M_1$ polytype in hydrothermally altered igneous rocks, where it occurs as a component of sericite (Eberl et al., 1987; Yan et al., 2001).

Pevear (1992) proposed the concept called "Illite Age Analysis" (IAA), which is based on dating of multiple size fractions and extrapolating an obtained function (age value vs. mass fraction of detrital illite) to zero detrital illite to get the age of the authigenic illite in a sample and to 100% detrital illite to get the age of the non-authigenic illite. One of the underlying assumptions in IAA is that the two end members should concentrate in different size fractions. Furthermore, age value was assumed to be linearly correlated with end-member mass fraction. As pointed out by Środoń (1999) and Szczerba and Środoń (2009), deviation from linearity of age value vs. fraction of detrital illite can be caused by different amounts of K in the two components and the logarithmic nature of the age equation. Szczerba and Środoń (2009) proposed an approach that takes into consideration both of these issues and developed the *MODELAGE* computer program to calculate end-member ages for two-component mixtures.

Clay gouges are common in the Tatra Mountains (a part of the Inner Western Carpathians on the Polish-Slovakian border), where they have been formed in shear zones developed in granitoids. The geology of the Tatra Mountains is quite well established (Jurewicz, 2005; Plašienka et al., 1997), but the mineral composition of the gouges has never been investigated.

The aims of the present study were to determine the mineralogy of selected clay gouges from the Tatra Mountains, to interpret their origins, and to obtain time constraints on the formation of the authigenic micaceous components of the gouges. Furthermore, an attempt was made to develop an approach capable of finding the ages in a three-component system.

Geological setting

The Tatra Mountains are the tallest mountains in the Inner Western Carpathians, which, in turn, comprise part of the Alpine orogenic system in Europe. The Tatras consist of a crystalline core, which is built of igneous (mainly granitic) and metamorphic rocks, and sedimentary cover thrust over the core during late Cretaceous stages of the Alpine Orogeny (Plašienka et al., 1997). The present study focused on the eastern part of

https://doi.org/10.1007/s42860-022-00176-7 Published online by Cambridge University Press

the range, the so-called High Tatras. According to Gawęda (2007), the composition of the biotite monzogranites, which are the most common type of granitoids in the High Tatras, is as follows: plagioclase (43–69%), quartz (21–29%), K-feldspar (0.8–24%), biotite (2–5%), and muscovite (0.4–2.9%). Muscovite occurs as a magmatic mineral, and alongside other varieties of dioctahedral micas occurs in the form of sericite within altered feldspars.

Geologic evolution of the Tatra Mountains

Granitoids of the Tatra Mountains are polygenetic, with several batches of granitoid magma having intruded between ~370 and 340 Ma (Burda et al., 2011, 2013; Gawęda et al., 2005, 2014). U-Pb dating of apatite returned the most-recent dates at ~340 Ma, which means that the granitoids have not experienced temperatures above the closure temperature of the U-Pb system in apatite, i.e. above 350–550°C, since 340 Ma (Gawęda et al., 2014). The earliest dates recorded by ^{40}Ar-^{39}Ar dating of white micas from mylonitization zones within the crystalline core are Variscan (~333 Ma; Maluski et al., 1993). These dates, however, could reflect post-magmatic extension (Gawęda et al., 2014). The core was uplifted and eroded during the Permian and the Early Triassic (Jurewicz, 2005). Subsequent transgression resulted in sedimentation of various siliciclastic sediments and carbonates that prevailed during the Mesozoic. Tectonic activity during this Era comprised Middle to Late Triassic rifting and extension, and a major thrusting and nappe-forming Alpine event in the Late Cretaceous (Jurewicz, 2005; Králiková et al., 2014; Plašienka et al., 1997). Mylonites from the Tatra Mountains and adjacent areas returned ^{40}Ar-^{39}Ar ages of the latter tectonic phase in the 75–89 Ma range (Maluski et al., 1993). Evidence of an earlier, Early Cretaceous thermotectonic event in the 140–120 Ma range was also found (Maluski et al., 1993). As inferred from a fluid inclusion study, temperatures of Alpine deformation for selected shear zones within the Tatra granitoid core did not exceed 250°C (Jurewicz & Kozłowski, 2003). The early Cenozoic evolution of the Tatra Mountains is difficult to determine because no sediments from that period lay directly on the crystalline core (Anczkiewicz et al., 2015), but zircon fission track (ZFT) ages of 77 ±11 to 63±6 Ma (Králiková et al., 2014) suggest a period of cooling and probable erosion. The final uplift took place in the Miocene (~20 Ma) and was preceded by late Eocene–Oligocene burial that started at about 45 Ma (Králiková et al., 2014). Anczkiewicz et al. (2015) and Śmigielski et al. (2016) demonstrated, by thermal history modeling based on ZFT and apatite fission track (AFT) ages, that temperatures during Paleogene burial were >150°C. AFT ages of crystalline-core samples are scattered from 15 to 30 Ma, which may indicate that the final uplift of the core involved block tectonics (Anczkiewicz et al., 2015). AFT dates record uplift from the 100°C isotherm, i.e. a depth of 5 km assuming a 20°C/km geothermal gradient.

Clay gouges

Clay gouges in the Tatra Mountains occur mainly along steeply dipping shear zones that were formed during pre-Alpine times (Jurewicz, 2006) and are accompanied by mylonites and cataclasites. Shear zones in the Tatra Mountains and surrounding areas have probably undergone multiple episodes of re-activation, as can be inferred from ^{40}Ar-^{39}Ar dating of fault-associated rocks that revealed Late Cretaceous and Paleogene ages (Kohút & Sherlock, 2003; Maluski et al., 1993) and from tectonic reconstruction models that imply final uplift of the High Tatras in the Neogene (Anczkiewicz, 2015; Jurewicz, 2005; Králiková, 2014).

Materials and methods

Samples used in the present study were collected from clay gouges developed in Variscan granitoids in the eastern part of the Tatra Mountains. Eight shear zones were investigated (Fig. 1; Table 1): Plecy Mnichowe (TM1), Mała Galeria Cubryńska (TM2), Żleb Mnichowy (TM3), Przełęcz za Zadnim Mnichem (TM4), Wrota Chałubińskiego (TM5), Gładka Przełęcz (TM6), Kozia Przełęcz (KP), and Zachód Grońskiego (ZG). All of the samples were taken from the zones that strike NE–SW. The ~0.5 m thick gouge TM4 was sampled along a cross section perpendicular to the walls in order to determine the variability of the mineral composition within the gouge (Fig. 2).

Sample handling and instrumental methods

Collected samples were air-dried and subsequently hand-crushed gently in a steel mortar to pass through a

https://doi.org/10.1007/s42860-022-00176-7 Published online by Cambridge University Press

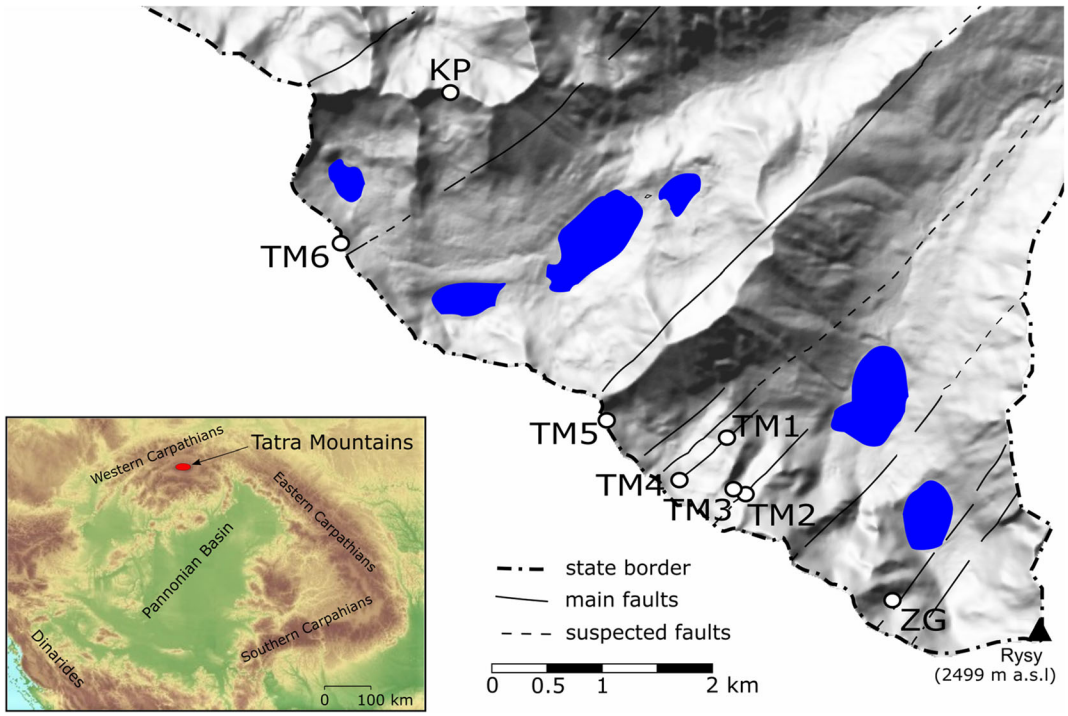

Fig. 1 Digital elevation model (DEM) of the area of study with sampling sites (white dots). Lakes shown in blue. Fault lines after Piotrowska (1970). Inset: DEM of the Carpathians showing the location of the Tatra Mountains (source: European Environment Agency, GTOPO 30 elevation model)

0.4 mm sieve. Prior to clay separation, portions of the ground samples were treated with Na acetate–acetic acid buffer to remove carbonates and exchangeable divalent cations (Jackson, 1969). The white to greenish-white color of the samples indicated a small organic matter content and small "free Fe-oxide" content, so peroxide and citrate-bicarbonate-dithionite treatments were not applied. After removal of carbonates and Na-saturation by four washings with 1 M NaCl (analytical reagent grade, POCH S.A., Gliwice, Poland), <0.2 μm size fractions were separated by centrifugation (Stokes's Law). For one sample, which was selected for the radiometric dating, three additional size fractions were separated by centrifugation (0.2–2 μm) or by sedimentation in a water column (2–10 μm and 10–20 μm) (Stokes's Law). Subsequently, fractions to be examined by X-ray diffraction (XRD) were saturated with Ca^{2+} or K^{+} cations by four washings with the respective chloride solutions (analytical reagent grade, POCH S.A., Gliwice, Poland). The final saturation was followed by dialysis to remove excess electrolytes.

Portions of the hand-crushed bulk samples were micronized with a McCrone micronizing mill (McCrone Microscopes & Accessories, Westmont, Illinois, USA), with 10% zincite (analytical reagent grade, Fisher Scientific, Waltham, Massachusetts, USA) added as an internal standard, and side-loaded into aluminum holders for XRD analysis. Portions of the size fractions (<0.2, 0.2–2, 2–10, and 10–20 μm) of the KP sample were loaded in similar fashion but with no internal standard. Clay fractions were also analyzed by XRD as oriented mounts on glass slides (with surface density of 10 mg/cm^2).

X-ray diffraction patterns were recorded using a Philips X'Pert APD system (Philips Electronics N.V., Almelo, The Netherlands) with a PW3020 goniometer equipped with a 1° divergence slit, a 0.02 mm receiving slit, a 2° antiscatter slit, a graphite diffracted-beam monochromator, and two Soller slits. CuKα radiation produced with an acceleration voltage of 40 kV and 30 mA current was used. The oriented mounts were scanned in a step scanning mode in the range of 2–52°2θ with 2 s counting time per 0.02°2θ step. The scanning range for random powder mounts was 2–65°2θ with 5 s counting time per 0.02°2θ step.

Quantitative analysis (qXRD) of bulk samples and the KP size fractions was performed with *Profex-BGMN* (Doebelin & Kleeberg, 2015) Rietveld refinement

https://doi.org/10.1007/s42860-022-00176-7 Published online by Cambridge University Press

Table 1 Locations and descriptions of the samples used in the study

Symbol	Sampling site	Coordinates	Description
TM1	Path to Plecy Mnichowe	49°11'45"N 23°06'09"E	Narrow (~15 cm) fault gouge of brownish color
TM2	Galeria Cubryńska	49°11'26"N 23°03'16"E	Thin (~5 cm) vein of gray-bluish clay material within mylonitic fault rock.
TM3	Żleb Mnichowy	49°11'26"N 20°03'08"E	Narrow (~10 cm) fault gouge of bluish-gray color, containing a relatively large number of pieces of crushed wall rock. Blurred boundaries.
TM4a TM4b TM4c TM4d	Przełęcz Za Zadnim Mnichem	49°11'21"N 20°05'09"E	Relatively wide (50–70 cm) fault gouge. Clay material within the gouge was of light-gray color with irregular veins of white variety. Quartz and carbonate veins 50 cm wide were close to the gouge. Four samples from a transect perpendicular to the boundaries were taken ~15 cm apart.
TM5	Wrota Chałubińskiego	49°11'30"N 20°02"43"E	Relatively wide (1.5 m) fault gouge with small number of pieces of wall rock and with blurred boundaries. Fresh material was gray-beige.
TM6	Gładka Przełęcz	49°12'29"N 20°00'44"E	Fault gouge ~50 cm wide of light beige color.
KP	Kozia Przełęcz	49°13'09"N 20°01'15"E	Very narrow (1–1.5 cm) clay gouge with sharp boundaries, almost white.
ZG	Zachód Grońskiego	49°10'57"N 20°04'35"E	Relatively wide (40–60 cm) homogeneous clay gouge with sharp boundaries and light green color. Visible fragments of wall rock in the center of a more clayey vein.

software. The region below 10°2θ was excluded from the refinement and the background polynomial order was constrained to 2.

Clay minerals present in the <0.2 μm size fractions were identified using the criteria given by Środoń (2013) for XRD patterns of oriented specimens. Smectite was identified by the presence of a 15 Å peak for the Ca^{2+} saturated air-dried form that shifts to ~17 Å upon saturation with ethylene glycol. Illite and chlorite were identified from 10 Å and 14 Å peaks, respectively, that do not shift upon saturation with ethylene glycol. For the samples TM4a, TM4b, TM4c, TM4d, and KP, the XRD patterns of oriented mounts were modeled with *Sybilla* (Chevron proprietary) software. During modeling, the region below 4°2θ was excluded from analysis because of large instrumental and interparticle diffraction effects (e.g. Drits & Tchoubar, 1990; Moore & Reynolds, 1997). The σ* parameter was set to 12 for all phases used. The charge of the illite particles in mixed-layered phases was assumed to be 0.95 per half unit cell and that of smectite was constrained to 0.41 after Środoń et al. (2009). The interplanar spacing (d_{001}) of illite and of the illitic component in illite-smectite (I-S) phases was fixed at 9.98 Å. The presence of smectitic layers with almost exclusively two glycol layers was assumed for glycol-saturated specimens. A highly smectitic I-S was used instead of pure smectite to model swelling phases present in the samples, following the approach of McCarty et al. (2009). The low-angle parts of the XRD patterns (<10°2θ) were allowed to have poorer fits in order to obtain better fits in the region between 24.5 and 27°2θ, which carries the most information on percentage of smectite and size distribution of the modeled phases (Środoń et al., 2009).

For potassium determination, portions of selected size fractions were digested in a sulfuric acid–hydrofluoric acid mixture, followed by hydrochloric acid treatment. The potassium content of the solutions obtained was measured with a Sherwood 420 flame photometer (Sherwood Scientific Ltd., Cambridge, UK) calibrated against NIST standards SRM 76a and SRM 70a. The measurement error of the photometric analysis corresponded to a 1σ uncertainty in clay K_2O content of ±0.05%, absolute.

Fourier-transform infrared (FTIR) spectra of Ca-saturated size fractions <0.2 μm were obtained from thin films deposited on top of the attenuated total reflectance (ATR) crystal using a Nicolet 6700 (Thermo Scientific, Waltham, Massachusetts, USA) FTIR

https://doi.org/10.1007/s42860-022-00176-7 Published online by Cambridge University Press

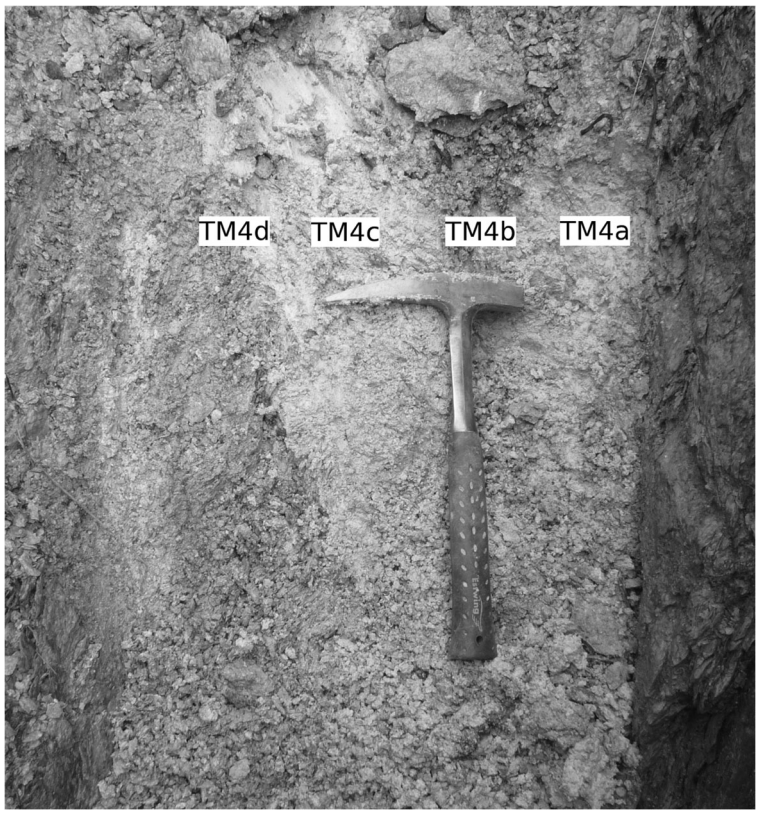

Fig. 2 Clay gouge TM4 situated in the Przełęcz za Zadnim Mnichem with sampling points

spectrometer equipped with a MIRacle (PIKE Technologies, Madison, Wisconsin, USA) ATR accessory following the procedure described by Kuligiewicz et al. (2015). Briefly, ~0.5 mg of a sample was dispersed in 0.5 mL of D_2O (99.9 atom% D, Sigma-Aldrich Chemie GmbH, Steinheim, Germany), and the suspension was deposited on top of the ATR crystal. Subsequently, the liquid was evaporated with a dry N_2 purge, which allowed us to obtain a FTIR spectrum free of interferences in the OH-stretching region from adsorbed H_2O molecules (Russell & Farmer, 1964). One hundred scans were collected for each sample in the range 400 to 4000 cm^{-1} with a resolution of 2 cm^{-1}. The spectra were smoothed using the Savitzky-Golay filter with a 17 point window.

Inspection of the results of the XRD analysis of bulk samples showed that the KP sample contained no feldspars, thus it was selected for ^{40}Ar-^{39}Ar dating. Four size fractions, <0.2, 0.2–2, 2–10, and 10–20 μm, saturated with Ca^{2+} were analyzed in the Ar-Ar Geochronology Laboratory of the University of Michigan following the analytical protocol of Hall (2014). Dated size fractions were saturated with Ca^{2+} in order to remove any loosely associated K^+ which could have been adsorbed on the surfaces of clay particles. Vacuum encapsulated samples were irradiated for 30 MWh at location 5C of the McMaster Nuclear reactor. Standard hornblende MMhb-1 was used as a neutron fluence monitor with an assumed age of 520.4 Ma (Samson & Alexander, 1987).

Encapsulated samples were not baked prior to analysis to avoid outgassing that might complicate measurement of the Ar released by the effects of recoil. Encapsulated samples were laser step-heated in situ for 60 s per step using a defocused beam from a 5 W Coherent Innova continuous Ar-ion laser operated in multi-line mode. Ar isotopes were measured using a VG1200S mass spectrometer with a source operating at 150 μA total emission and equipped with a Daly detector operating in analog mode. Mass discrimination was monitored daily using ~2 pmol of atmospheric Ar. A blank step (no heating) was run after every five heating steps and blank corrections — typically ~1 amol, ~1.4 amol, ~0.5 amol, ~1.4 amol, and ~90 amol — were applied to the amounts of the argon isotopes 36 through 40, respectively, determined in each gas fraction. Corrections

https://doi.org/10.1007/s42860-022-00176-7 Published online by Cambridge University Press

were also made for the decay of ^{37}Ar and ^{39}Ar; for the argon produced by interfering nuclear reactions from K, Ca, and Cl; and for production of ^{36}Ar from the decay of ^{36}Cl. The decay constants of ^{40}Ar and the atmospheric Ar isotopic composition are those of Steiger & Jäger (1977).

Age calculations

The results of radiometric dating were first interpreted using the IAA concept (Pevear, 1992) and an alternative approach based on *MODELAGE* software (Szczerba & Środoń, 2009) to estimate age values of authigenic and inherited components by extrapolation. IAA, modified by plotting values of $e^{\lambda t} - 1$ instead of age values, was performed using York regression (York et al., 2004) assuming that errors follow a normal distribution and are uncorrelated. In the case of mineralogical analysis, the 1σ error was assumed to be 5% (absolute), following the authors' experience in qXRD of clay-bearing materials. The alternative approach followed the age-calculation procedure of *MODELAGE* software, where the $I_{d(K)}$ parameter is used instead of the mass fraction of non-authigenic components in end-member age extrapolation (Eq. 3 of Szczerba & Środoń, 2009). $I_{d(K)}$ represents potassium within non-authigenic minerals of a size fraction as a percentage of the total amount of potassium in this size fraction. $I_{d(K)}$ is used in *MODELAGE* plots because, in principle, a plot of $^{40}Ar^{*}/^{40}K$ vs. percentage of non-authigenic illite is linear only if the K contents of the authigenic and non-authigenic illite are equal, which should not be assumed. The ratio $^{40}Ar^{*}/^{40}K$ instead of the age is used in order to overcome the departure from linearity of the $I_{d(K)}$ vs. age plot posed by the logarithmic nature of the age equation. The use of the $^{40}Ar^{*}/^{40}K$ ratio is equivalent to using $e^{\lambda t} - 1$ as proposed by van der Pluijm et al. (2001), because the two values are linearly related (Szczerba & Środoń, 2009). Although created for K-Ar dating results, the *MODELAGE* software can work equally well using the results of ^{40}Ar-^{39}Ar dating. It is because ^{40}Ar-^{39}Ar total-gas age values are equivalent to conventional K-Ar age values. *MODELAGE* software has an internal constraint that the calculated end-member ages have to be non-negative. In order to overcome this issue, calculations were made in the Microsoft Excel spreadsheet, following the approach implemented in the *MODELAGE* software. The Solver™ Excel add-in was used with a genetic optimization engine to refine three parameters: the ratio of $^{40}K_{authigenic}$ to $^{40}K_{non\text{-}authigenic}$ and age values of the two end members. Following the computational algorithm implemented in the *MODELAGE* software, theoretical $e^{\lambda t} - 1$ values for each size fraction were computed based on the three aforementioned variables and the results of qXRD analysis. These theoretical values were compared with the $e^{\lambda t} - 1$ values for each size fraction obtained by ^{40}Ar-^{39}Ar dating. The goal of optimization was to minimize the difference between these two data sets. During optimization, the $^{40}K_{authigenic}$ to $^{40}K_{non\text{-}authigenic}$ value was allowed to vary in the 0.7 to 1.5 range, and end-member ages were allowed to vary between –100 and 500 Ma. Errors around the end-member age values were determined with the Monte Carlo method under assumption of a normal error distribution about each measured value with standard deviation equal to the 1σ measurement uncertainty. Optimization was repeated 1000 times with randomly changed input variables.

Results and discussion

Bulk composition of the gouges

The most abundant components of the gouge samples were quartz, with contents varying between 33 and 52%, and dioctahedral mica (Table 2). The sum of the amounts of the dioctahedral 2:1 layer silicates in bulk gouge varied widely between 56% for sample TM4d and 24% for sample ZG, with the average about 44% (Table 2). Chlorite was a minor constituent (≤4%) of all samples. Plagioclase was abundant in some samples, a little K-feldspar was present in a few samples, and one sample contained discrete dioctahedral smectite (14%). Small amounts of calcite in some samples and a very small amount of anatase in one sample were also observed.

Composition of the <0.2 μm fractions

All fine-clay fractions separated from studied samples contained discrete illite, expandable dioctahedral phyllosilicates (I-S and discrete dioctahedral smectite), and chlorite, as evidenced by XRD patterns of oriented mounts (Fig. 3 and associated Research Data). In addition, the presence of a band at 3696 cm^{-1} in the FTIR spectra of samples TM4b, TM4d, TM5, and TM6 indicated the presence of small admixtures of kaolinite,

https://doi.org/10.1007/s42860-022-00176-7 Published online by Cambridge University Press

Table 2 Results of qXRD analysis (mass %) of bulk samples with the goodness of fit parameter R_{wp}

Sample	Quartz	Plagioclase	K-Feldspar	Mica $2M_1$	Mica $1M_d$	Mica $1M$	Chlorite	Dioctahedral Smectite	Calcite	Anatase	R_{wp} (%)
TM1	39.3	16.3	0.0	31.9	8.4	0.0	4.0	0.0	0.0	0.0	9.6
TM2	38.2	9.6	0.0	26.5	20.8	0.0	3.4	0.0	1.7	0.0	9.2
TM3	38.9	21.1	0.0	19.6	13.1	0.0	3.7	0.0	3.5	0.0	8.9
TM4a	49.7	0.5	0.0	33.7	8.3	4.1	3.6	0.0	0.0	0.0	9.0
TM4b	46.1	0.0	0.0	29.0	18.0	0.0	3.7	0.0	3.2	0.0	8.5
TM4c	47.3	0.0	0.0	30.8	15.5	5.2	1.0	0.0	0.3	0.0	9.3
TM4d	39.8	0.0	0.4	38.7	12.9	4.2	2.3	0.0	1.2	0.5	9.0
KP	41.8	0.0	0.0	23.8	28.4	0.0	1.8	0.0	4.2	0.0	8.4
TM5	47.1	0.9	0.2	24.6	10.5	0.7	1.7	14.2	0.0	0.0	8.5
ZG	32.5	37.8	3.2	15.3	8.4	0.0	2.9	0.0	0.0	0.0	9.0
TM6	52.4	0.0	0.0	22.7	12.7	10.0	2.2	0.0	0.0	0.0	9.0

which were below the XRD detection limit (Fig. 4). Modeling of the XRD patterns of a few of the fine-clay fractions with the *Sybilla* (Chevron proprietary) software indicated the presence of at least two illite and/or I-S populations (Table 3). The <0.2 μm fractions were dominated by 2:1 phyllosilicates, with prevailing mixed-layered I-S and discrete illite and minor amounts of chlorite. Kaolinite was not included in the modeling because it was present as a small admixture, detectable only by FTIR (Figs 3 and 4). In the case of the KP sample, the model that produced the best fit was relatively simple and contained only chlorite, illite, and highly illitic R1 I-S (8% smectite; Table 3). In the TM4 set of samples, two groups were distinguished. For samples TM4a and TM4b, models included highly illitic I-S and either highly smectitic (88%) I-S or discrete smectite. Models proposed for samples TM4c and TM4d contained two populations of ordered (R1), highly illitic I-S with different percentages of smectite. The remaining phases in both groups were discrete illite and chlorite (Table 3).

Quantitative analysis of size fractions of the KP sample

$1M_d$, $1M$, and $2M_1$ polytypes (of dioctahedral mica and/or illite) were identified in <0.2, 0.2–2, 2–10, and 10–20 μm size fractions separated from the KP sample, based on the presence of diagnostic reflections in the 20–30°2θ range in the XRD patterns of random powder mounts (Fig. 5). Because these size fractions were selected for ^{40}Ar-^{39}Ar dating, a detailed quantification of the relative proportions of these polytypes was performed. While $1M$ and $2M_1$ structures are described adequately by default structure files available in the *Profex-BGMN* database, the $1M_d$ structure is simplified, which may cause imprecise quantification. Therefore, the $1M_d$ structure description provided by Ufer et al. (2012) was used instead. This structure allowed simulation of peak broadening resulting from the presence of 60° and/or 120° rotations along the c* crystallographic direction and *cis* and *trans* vacancies in the octahedral sheet. Tests performed for $1M_d$ structures containing 120° rotations and both 120° and 60° rotations, both with and without preferred orientation (Table S1), revealed that the differences in relative proportions of different polytypes among quantifications based on different $1M_d$ structural models were smaller than the qXRD error assumed to be 5% (absolute). The exception was the quantification using the $1M_d$ structure with 120° rotations without preferred orientation for the <0.2 μm size fraction. This model was considered as oversimplified, because it was the one that returned results inconsistent with the three other quantifications for this size fraction (Table S1). Generally, the amount of the $1M_d$ polytype decreased systematically from the finest to the coarsest size fraction. The $2M_1$ polytype displayed the opposite trend, and the $1M$ content remained relatively constant among size fractions.

Given the similarity of the results obtained with the three models considered as reliable, quantification involving the $1M_d$ illite model with 120° rotations and preferred orientation was used in further considerations (Table 4). This model was chosen over the two models that include 60° rotations because, in XRD patterns of

https://doi.org/10.1007/s42860-022-00176-7 Published online by Cambridge University Press

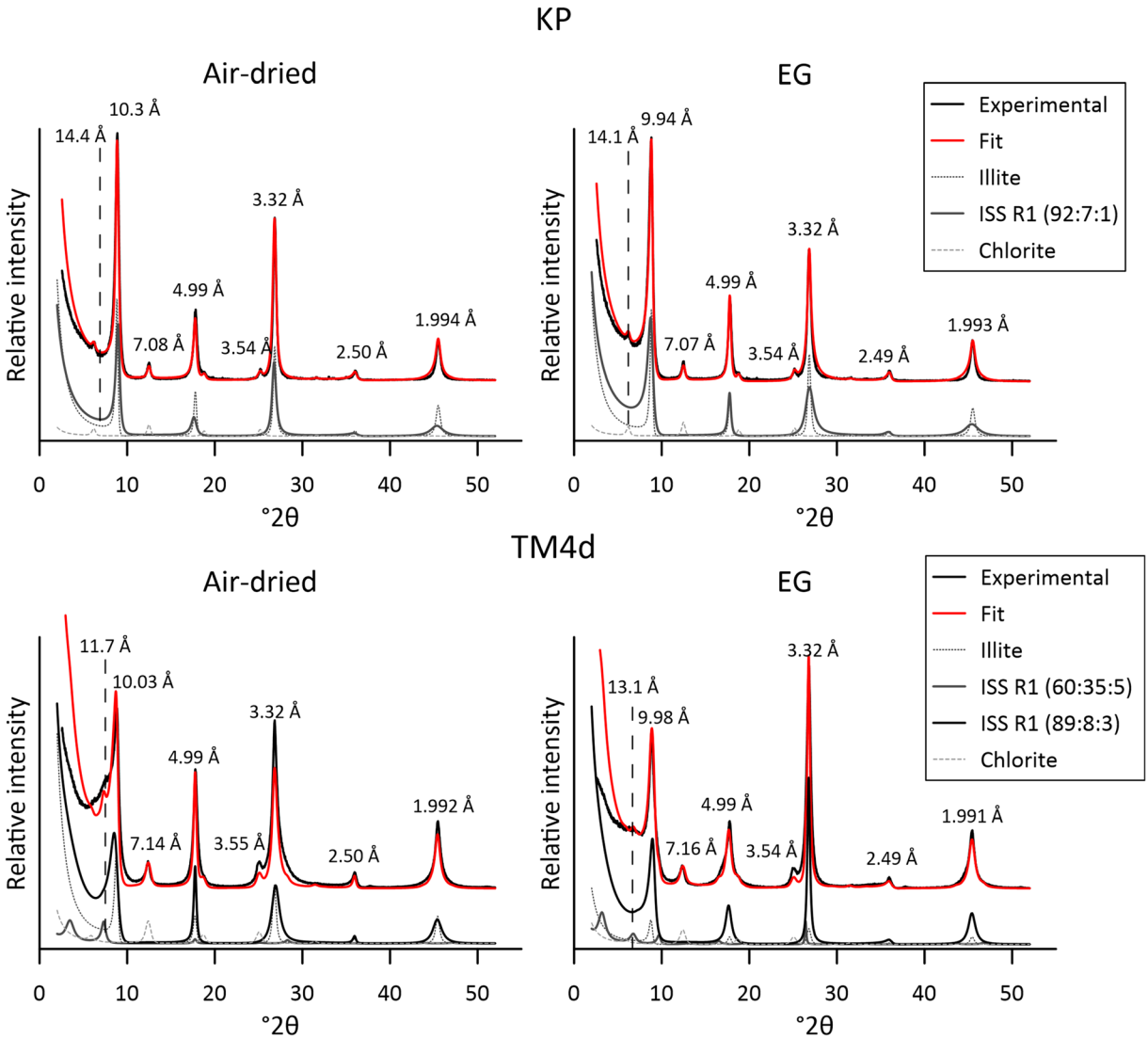

Fig. 3 XRD patterns of oriented mounts for <0.2 μm fractions of the KP (top) and TM4d (bottom) samples with theoretical models calculated with *Sybilla* (Chevron proprietary) software. EG denotes patterns of ethylene glycol-solvated clay

examined samples, separate reflections in the 37–39°2θ range were observed, which is characteristic for structures that do not contain 60° rotations (Fig. 5). If such rotations were present, only one broad reflection should be observed in the 37–39°2θ range instead.

Problems associated with polytype quantification

Precise quantification of polytypes can be affected by several problems. Relative amounts of 1*M* and 1M_d polytypes can depend on definition of these structures. Theoretically, if a structure of 1M_d polytype with reflections similar to those of 1*M* is used, part of the XRD intensity in the regions of overlap is assigned to the 1M_d polytype, which leads to reduction in the amount of 1*M* polytype in quantification. For example, Grathoff and Moore (1996) assumed that the 1M_d polytype contains 60% *trans*- and 40% *cis*-vacant layers; the fraction of 0° rotations is 0.6; and the fraction of 60°, 180°, and 300° rotations is 0.6. This model results in reflections at 3.61 and 3.10 Å, similar to those of the 1*M* phase (Fig. 2 of Grathoff & Moore, 1996). In the case of the 1M_d polytype of the KP sample in the present study, no 60°, 180°, and 300° rotations were assumed, and BGMN was allowed to optimize *trans*- vs. *cis*-vacant layer contents and fraction of 0° rotations for each size fraction separately. This led also

https://doi.org/10.1007/s42860-022-00176-7 Published online by Cambridge University Press

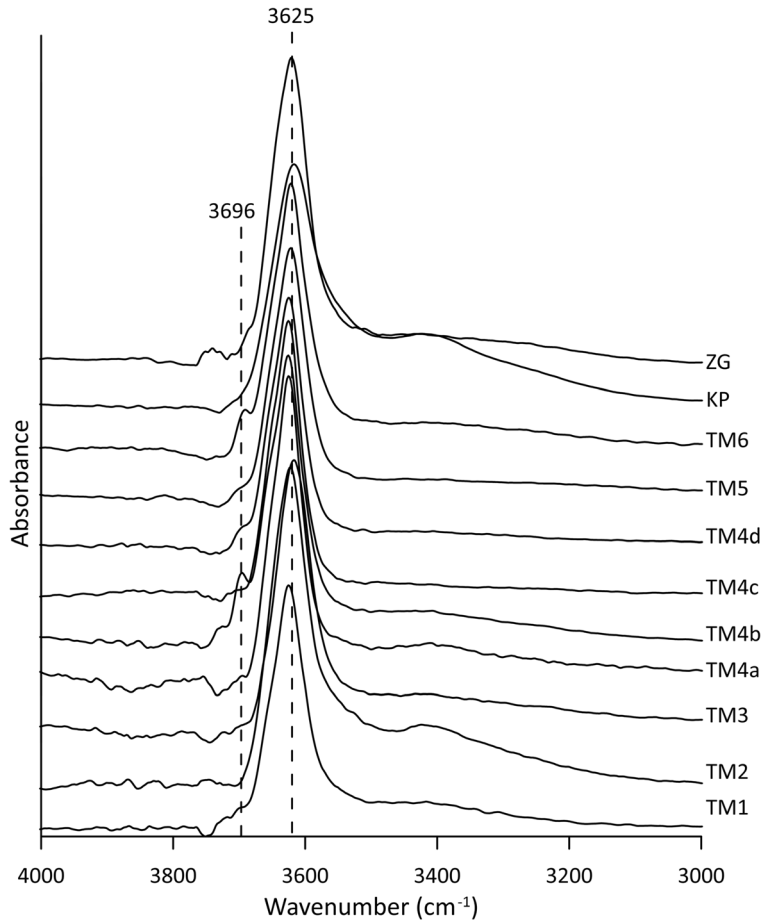

Fig. 4 FTIR spectra of fine-clay fractions of the investigated samples. The band at 3696 cm^{-1}, at the side of the main OH-stretching envelope of dioctahedral 2:1 phyllosilicates at ~3625 cm^{-1}, indicates the presence of kaolinite

to some overlap of reflections of 1*M* and $1M_d$ phases at ~24 and 27°2θ (Fig. 5). Refined structures for the $1M_d$ polytype (Table 5) were somewhat different from those assumed by Grathoff and Moore (1996). Generally, there were fewer 0° rotations, which means that XRD patterns of the $1M_d$ polytype had more diffuse reflections. The $1M_d$ structures were also more dominated by *trans*-vacant layers.

The crystallinity of all phases is another important factor, because samples with larger crystallites produce more intense reflections than compositionally equivalent samples with smaller crystallites. In the case of polytype quantification, the larger the crystallites of a polytype, the smaller the amount of that polytype required to fit the experimental XRD pattern of a sample.

^{40}Ar-^{39}Ar dating

The smaller age values of finer size fractions (Fig. 6) pointed toward tentative acceptance that a basic assumption of ^{40}Ar-^{39}Ar radiometric dating of clay mixtures was fulfilled, i.e. that the younger, authigenic component has smaller crystallites and is relatively concentrated in finer size fractions (Kelley, 2002). None of the Ar-release patterns exhibited a plateau (Fig. 6). This behavior is typical of very fine material and does not invalidate the dates obtained (Haines & van der Pluijm, 2008). Total-gas age values instead of retention age values were used because samples were Ca-exchanged before radiometric dating, which makes valid the assumption that no weakly bonded potassium is present in the non-retentive sites. Using total-gas age values is appropriate under this assumption (van der Pluijm & Hall, 2015). In addition, total-gas age values are equivalent to conventional K-Ar age values. The age values of authigenic and inherited material were calculated under the assumption that the $1M_d$ polytype is authigenic and that the 1*M* and $2M_1$ polytypes were inherited. That the 1*M* polytype was inherited from the wall rocks seemed likely, because formation of this polytype as an

https://doi.org/10.1007/s42860-022-00176-7 Published online by Cambridge University Press

Table 3 Parameters of *Sybilla* (Chevron proprietary) models for <0.2 μm Ca^{2+}-exchanged and ethylene glycol-saturated fractions of selected samples

Sample	Composition	
	Phase	Amount (%)
KP	Illite	45
	ISS R1 (92:7:1)	53
	Chlorite	2
TM4a	ISS R0 (12:76:12)	6
	ISS R1 (90:10:0)	44
	Illite	47
	Chlorite	3
TM4b	SS (87:13)	4
	ISS R1 (89:9:2)	70
	Illite	22
	Chlorite	4
TM4c	ISS R1 (58:36:6)	9
	ISS R1 (88:11:1)	71
	Illite	19
	Chlorite	1
TM4d	ISS R1 (60:35:5)	6
	ISS R1 (89:8:3)	82
	Illite	10
	Chlorite	2

authigenic clay gouge component is not widely documented (Haines & van der Pluijm, 2012).

The results obtained for authigenic and inherited components using the IAA concept were −14±31 and 180±91 Ma for authigenic and inherited components, respectively. The average age values obtained by Monte Carlo calculations in the *MODELAGE*-based approach (hereinafter *MODELAGE* approach) were −4±40 and 165±62 Ma for authigenic and inherited components, respectively. The ratio of potassium content in authigenic and non-authigenic components ($^{40}K_{authigenic}/^{40}K_{non\text{-}authigenic}$) was 1.1±0.2. Results for particular Monte Carlo runs are presented in Table S2.

Calculation of K contents and age values in a three-component system

Potassium contents of size fractions separated from the KP sample varied from 6.89 to 8.52% (as K_2O) and were inversely correlated with the particle size (Table 4). The examined material contained three dioctahedral mica and/or illite polytypes ($1M_d$, $1M$, and $2M_1$) which might differ from one another in age and K_2O content. Following the reasoning of Szczerba & Środoń (2009), determination of the K_2O content of each polytype is an important prerequisite for age determination. Assuming that each polytype has the same

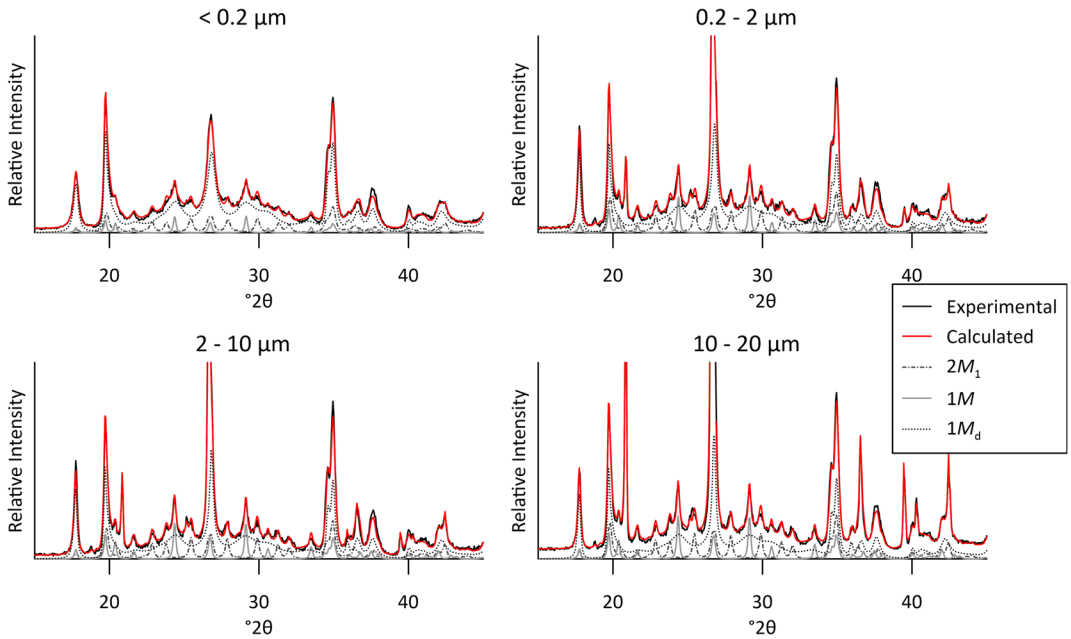

Fig. 5 XRD patterns of random powder mounts of different size fractions of the KP sample with theoretical patterns calculated with *BGMN-Profex* software

https://doi.org/10.1007/s42860-022-00176-7 Published online by Cambridge University Press

Table 4 qXRD analysis results and K_2O contents (all as percent by mass) of size fractions of the KP sample. See text for estimates of the analytical errors

Size fraction (μm)	Mica $1M_d$	Mica $1M$	Mica $2M_1$	Quartz	Chlorite	Smectite	Sum of non-illite components	Sum	K_2O
<0.2	70.6	6.7	16.2	0.5	1.5	4.4	6.4	99.9	8.52
0.2-2	54.7	12.1	20.3	9.3	3.5	0.0	12.8	99.9	8.50
2-10	53.9	12.8	19.1	10.7	3.6	0.0	14.3	100.1	8.38
10-20	40.7	10.9	16.4	30.1	1.9	0.0	32.0	100.0	6.89

K_2O content in each size fraction, the following set of linear equations is obtained:

$$w_1 f_{1a} + w_2 f_{2a} + w_3 f_{3a} = w_a \quad (1a)$$

$$w_1 f_{1b} + w_2 f_{2b} + w_3 f_{3b} = w_b \quad (1b)$$

$$w_1 f_{1c} + w_2 f_{2c} + w_3 f_{3c} = w_c \quad (1c)$$

$$w_1 f_{1d} + w_2 f_{2d} + w_3 f_{3d} = w_d \quad (1d)$$

where f stands for the mass fraction of a given polytype in a size fraction as determined with qXRD (Table 4), w stands for the mass fraction of K_2O in a polytype or in a size fraction, subscripts 1, 2, and 3 denote the $1M_d$, $1M$, and $2M_1$ polytypes, respectively, and subscripted letters indicate the size fraction: a – <0.2 μm; b – 0.2–2 μm; c – 2–10 μm; d – 10–20 μm; e.g. f_{1a} stands for the mass fraction of the $1M_d$ polytype in the <0.2 μm size fraction. The symbols $w_a - w_d$ denote the mass fractions of K_2O in size fractions a to d, respectively (Table 4).

The matrix inversion technique was applied in order to facilitate handling of the set of linear equations with three unknowns (Collins, 1990). This method is applicable to sets of equations with an equal number of equations and unknowns. Three subsets of Eq. 1 having three equations each were selected for matrix inversion. These were Eqs 1a, 1b, and 1c; 1a, 1b, and 1d; 1a, 1c, and 1d. The subset of Eqs 1b, 1c, and 1d was not used, because it had very small differences in polytype contents. The set of Eq. 1a, 1b, and 1c can be written in matrix form as:

$$\begin{bmatrix} f_{1a} & f_{2a} & f_{3a} \\ f_{1b} & f_{2b} & f_{3b} \\ f_{1c} & f_{2c} & f_{3c} \end{bmatrix} \begin{bmatrix} w_1 \\ w_2 \\ w_3 \end{bmatrix} = \begin{bmatrix} w_a \\ w_b \\ w_c \end{bmatrix} \quad (2)$$

Analogous equations can be written for the remaining subsets. The first matrix on the left in Eq. 2 contains mass fractions of polytypes in size fractions <0.2, 0.2–2, and 2–10 μm. If the determinant of this matrix is other than 0, both sides of Eq. 2 can be multiplied by the inverse fraction matrix. This was the case for all subsets. The inverse matrix equation for the subset 1a-1b-1c is, therefore,

$$\begin{bmatrix} w_1 \\ w_2 \\ w_3 \end{bmatrix} = \begin{bmatrix} f_{1a} & f_{2a} & f_{3a} \\ f_{1b} & f_{2b} & f_{3b} \\ f_{1c} & f_{2c} & f_{3c} \end{bmatrix}^{-1} \begin{bmatrix} w_a \\ w_b \\ w_c \end{bmatrix} \quad (3)$$

An analogous transformation was made for the two remaining subsets.

Table 5 Detailed structural parameters of dioctahedral mica and/or illite polytypes obtained by *Profex-BGMN* optimization. B1 – crystallite size parameter, p0 – fraction of 0° rotations, pcv – fraction of *cis*-vacant layers. Parameters p0 and pcv were refined only for the $1M_d$ polytype

Polytype		$1M_d$			$1M$	$2M_1$
Parameter		B1	p0	pcv	B1	B1
Fraction	< 0.2 um	0.00555	0.502	0.398	0.0090	0.01185
	0.2-2 um	0.00258	0.3884	0.141	0.00913	0.01437
	2-10 um	0.00228	0.481	0.269	0.01136	0.01021
	10-20 um	0.00228	0.406	0.072	0.00722	0.00972

https://doi.org/10.1007/s42860-022-00176-7 Published online by Cambridge University Press

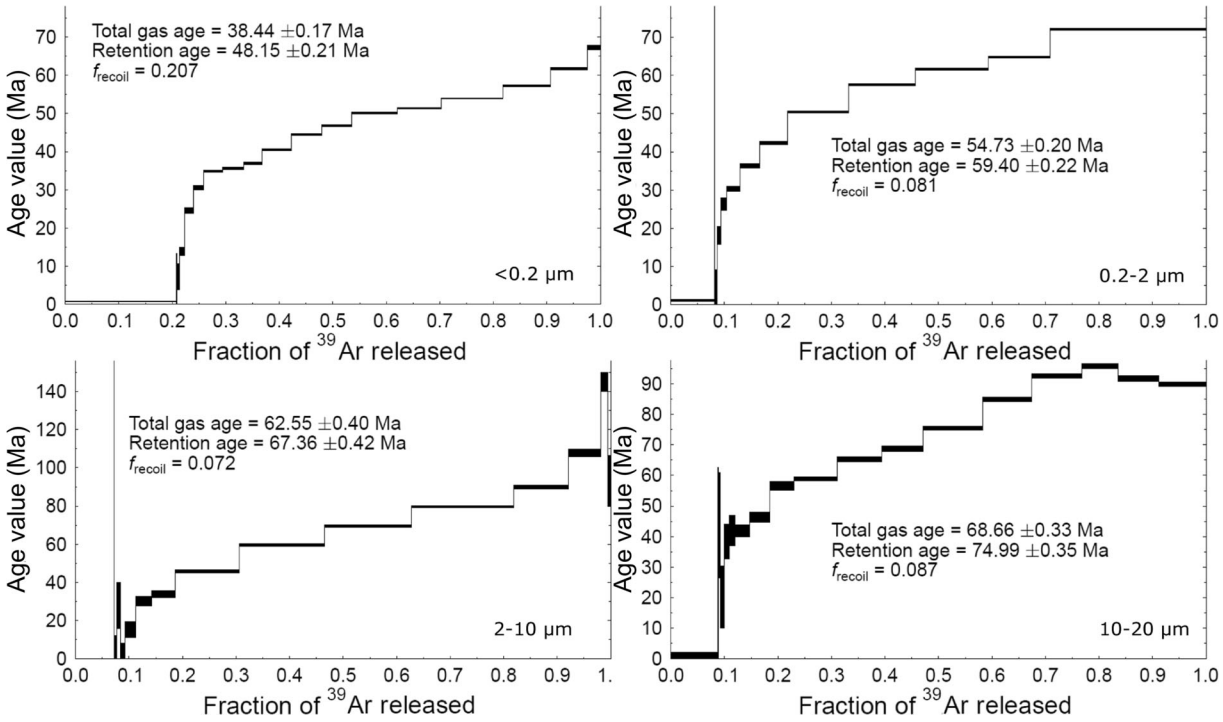

Fig. 6 Ar-release patterns of dated size fractions

Once a value for the K_2O content of each polytype is known, calculation of a K-Ar age value for each polytype is possible. The ^{40}K content of a size fraction is given by

$$^{40}\mathrm{K} = f_1\,{}^{40}\mathrm{K}_1 + f_2\,{}^{40}\mathrm{K}_2 + f_3\,{}^{40}\mathrm{K}_3, \quad (4)$$

where ^{40}K denotes a specific amount (amount of substance per unit mass) of ^{40}K and f denotes mass fraction of a polytype as in Eq. 1. Similarly, for the radiogenic Ar content of a size fraction

$$^{40}Ar^* = f_1\,{}^{40}\mathrm{Ar}_1^* + f_2\,{}^{40}\mathrm{Ar}_2^* + f_3\,{}^{40}\mathrm{Ar}_3^*, \quad (5)$$

where $^{40}Ar^*$ denotes a specific amount of radiogenic argon. The K-Ar method age equation yields

$$e^{\lambda t} - 1 = \frac{\lambda}{\lambda_{\mathrm{Ar}}}\left[\frac{^{40}\mathrm{Ar}^*}{^{40}\mathrm{K}}\right]. \quad (6)$$

Substitution of Eq. 5 into Eq. 6 gives a relationship that may be expressed as

$$e^{\lambda t} - 1 = \frac{\lambda}{\lambda_{\mathrm{Ar}}}\left[\frac{f_1\,{}^{40}\mathrm{K}_1}{^{40}\mathrm{K}}\frac{^{40}\mathrm{Ar}_1^*}{^{40}\mathrm{K}_1} + \frac{f_2\,{}^{40}\mathrm{K}_2}{^{40}\mathrm{K}}\frac{^{40}\mathrm{Ar}_2^*}{^{40}\mathrm{K}_2} + \frac{f_3\,{}^{40}\mathrm{K}_3}{^{40}\mathrm{K}}\frac{^{40}\mathrm{Ar}_3^*}{^{40}\mathrm{K}_3}\right], \quad (7)$$

which leads to

$$e^{\lambda t} - 1 = \frac{f_1\,{}^{40}\mathrm{K}_1}{^{40}\mathrm{K}}\left(e^{\lambda t_1} - 1\right) + \frac{f_2\,{}^{40}\mathrm{K}_2}{^{40}\mathrm{K}}\left(e^{\lambda t_2} - 1\right) + \frac{f_3\,{}^{40}\mathrm{K}_3}{^{40}\mathrm{K}}\left(e^{\lambda t_3} - 1\right). \quad (8)$$

Despite the fact that atomic proportions of ^{40}K in the polytypes and in the size fractions are used in Eq. 8, potassium contents can be used instead, because the relative abundance of ^{40}K in common terrestrial materials is virtually constant, i.e. one may assume that $^{40}K/K_2O$ in each polytype and in each size fraction is the same. Assuming that the age value of each polytype is constant among size fractions, following from Eq. 8 is that (for subsystem 1a-1b-1c; notation as in Eq. 1):

https://doi.org/10.1007/s42860-022-00176-7 Published online by Cambridge University Press

$$\begin{bmatrix} e^{\lambda t_1}-1 \\ e^{\lambda t_2}-1 \\ e^{\lambda t_3}-1 \end{bmatrix} = \begin{bmatrix} \frac{f_{1a}w_1}{w_a} & \frac{f_{2a}w_2}{w_a} & \frac{f_{3a}w_3}{w_a} \\ \frac{f_{2a}w_1}{w_b} & \frac{f_{2b}w_2}{w_b} & \frac{f_{3b}w_3}{w_b} \\ \frac{f_{3a}w_1}{w_c} & \frac{f_{2c}w_2}{w_c} & \frac{f_{3c}w_3}{w_c} \end{bmatrix}^{-1} \begin{bmatrix} e^{\lambda t_a}-1 \\ e^{\lambda t_b}-1 \\ e^{\lambda t_c}-1 \end{bmatrix} \quad (9)$$

Analogous equations can be written for the two remaining subsets of Eq 1.

An attempt was made to calculate K_2O contents and age values of the three mica and/or illite polytypes identified in sample KP using the logic described above. The set of four equations with three unknowns (w_1, w_2, and w_3; Eq 1) is inconsistent after substitution of mineralogical and chemical data for the KP sample, i.e. no set of w_1, w_2, and w_3 values exists that simultaneously satisfies all equations. Furthermore, different K_2O contents and age values are obtained for corresponding polytypes when data are substituted into Eqs 3 and 9 written for different subsets of Eq. 1. This is interpreted as a result of analytical errors, mainly the error of qXRD, which is two orders of magnitude greater than the error of K determination. An attempt was made to remove the inconsistency by optimization of the analytical results, allowing measured values to vary within ranges defined by their 1σ measurement uncertainty. An Excel spreadsheet with Solver™ add-in was used to simultaneously minimize (1) the sum of squared differences in K_2O contents obtained for each polytype with different subsets of Eqs 1 and (2) the sum of squared differences in age values obtained for each polytype with different subsets of Eq. 1. The mass fraction of each polytype and the sum of mass fractions of K-free phases in size fractions were allowed to vary in the ±5% range. Optimized size fraction compositions had to sum to 100%. The K_2O content of each size fraction was allowed to vary within the ±0.05% range, corresponding to the 1σ measurement error of K_2O determination. Similarly, age values of size fractions were optimized in the range defined by the 1σ analytical uncertainty of the ^{40}Ar-^{39}Ar analysis. The optimization allowed to obtain a set of data (Table 6), which returned consistent values for the K_2O contents and age values of the polytypes: w_1 = 8.77%, w_2 = 11.28%, and w_3 = 10.35%, t_1 = −6 Ma, t_2 = 205 Ma, and t_3 = 101 Ma for $1M_d$, $1M$, and $2M_1$ illite, respectively.

The above-mentioned K contents and age values for the polytypes are not associated with any estimate of uncertainty. In order to rectify this issue, a Monte Carlo approach was used. Calculations of K_2O contents and age values of polytypes were repeated 1000 times using randomly changed optimized input data (Table S3). For each repetition, values of polytype contents, K_2O content, and ^{40}Ar-^{39}Ar age for each size fraction were randomly drawn, each from a population having a normal distribution about the optimized value of that variable (Table 6) and a standard deviation equal to the 1σ measurement uncertainty, and substituted into Eqs 3 and 9. For each subset of Eq. 1, a small number of repetitions (between 2.7 and 3.3%) returned $e^{\lambda t} - 1$ values that were smaller than −1 and consequently could not be converted to Ma. These repetitions were discarded when analyzing age values of the polytypes.

Interestingly, the results obtained showed that w_1, w_2, and w_3, as well as age values of the $1M_d$, $1M$, and $2M_1$ polytypes do not have normal distributions (Table S4 and Fig. S1). This is confirmed by the results of the Shapiro-Wilk test, which returned p-values of <0.05 for K_2O contents and age values of the polytypes generated by the Monte Carlo calculations (Table S4). Visual inspection of histograms of K_2O contents and age values of the polytypes points toward a Cauchy (Lorentz) distribution, i.e. symmetric distribution with very long tails on both sides of the maximum (Fig. S1). In such a situation, statistical measures other than the mean and the standard deviation are needed to provide an accurate description of data. For this reason, the median and the interquartile range (IQR) were used for the central value and the uncertainty range, respectively, of calculated age values in the three-component system. The results (median values) of the Monte Carlo approach differed from results of initial optimization; however, the former

Table 6 Optimized mineralogical composition (mass %), K_2O content, and age value for various size fractions of the KP sample

Size fraction (μm)	Mica $1M_d$	Mica $1M$	Mica $2M_1$	K-free	K_2O (%)	Age value (Ma)
<0.2	67.8	7.5	16.6	8.2	8.50	38.35
0.2–2	56.5	10.4	22.7	10.3	8.48	54.70
2–10	55.0	14.9	18.1	12.1	8.40	62.63
10–20	40.7	12.2	18.6	28.4	6.88	68.50

https://doi.org/10.1007/s42860-022-00176-7 Published online by Cambridge University Press

are considered as more reliable because results of the Monte Carlo approach can be associated with uncertainties based on their IQR ranges. The three-component age values used in further considerations are median values averaged across all subsets (Table 7). The associated uncertainties are based on correspondingly averaged IQR values and are presented as plus or minus one-half of the IQR.

No large differences were found in the median of calculated K_2O values among the polytypes. This result agreed with a $^{40}K_{authigenic}/^{40}K_{non\text{-}authigenic}$ ratio not differing significantly from 1, as calculated with the *MODELAGE* approach.

Comparison of age values calculated with various approaches

Both IAA and *MODELAGE* approaches returned negative age values of the authigenic component of the gouge. The time ranges of formation of the authigenic component, as defined by 1σ uncertainties, were −45 to 17 Ma and −44 to 36 Ma, for IAA and *MODELAGE* approaches, respectively. The earlier boundary of the range for the *MODELAGE* approach is close to the total gas age of the finest size fraction (38.44±0.17 Ma). In the three-component system, the age value for the $1M_d$ polytype was 15±37 Ma. All age values obtained for the youngest component of the gouge point towards post-Paleogene formation of this component, most probably during final Miocene uplift of the core, as indicated by the median values of $1M_d$ age calculated with the three-component approach (Table S4).

IAA and *MODELAGE* approaches returned age values for the inherited component of 180 and 165 Ma, respectively, with corresponding 1σ time ranges being 89−271 Ma, and 103−227 Ma. The three-component system returned age values of 135 Ma (IQR time range 78−192 Ma) and 121 Ma (IQR time range 65−177 Ma) for the $1M$ and $2M_1$ polytypes, respectively. Disregarding error, the age values for the inherited component coming from IAA and *MODELAGE* approaches correspond roughly to late Early Jurassic−Late Jurassic extension. Median age values for the $1M$ and $2M_1$ polytypes obtained with the three-component approach correspond to a thermotectonic event that was suggested to have affected the area around 140–120 Ma (Maluski et al., 1993). A definitive link of any component to a particular phase of tectonic activity in the area is, however, not possible because of large uncertainties around the calculated age values. An alternative explanation of such age values in the present work is that they are the result of partial resetting of the K-Ar system of micas formed during intrusion of Tatra granitoids 340–370 Ma by one or more of the subsequent tectonic events.

Table 7 Age values (Ma) calculated with the different approaches used in the present study

Polytype	$1M_d$	$1M$	$2M_1$
IAA	–14±31	180±91	
MODELAGE	–4±40	165±62	
Three-component approach	15±37	135±57	121±56

Interpretation of polytype age values obtained in the present study is highly speculative because of large uncertainties associated with those values. Several factors can possibly contribute to such large uncertainties. First, variability of polytype contents among separated size fractions is relatively small. In addition, the relative amount of the $1M$ polytype is small, which also amplifies the error in the three-component approach. In two-component approaches, a small variability of $2M_1$ + $1M$ polytype contents makes the regression upon which the age value calculation is based poorly constrained (Pevear, 1999; Szczerba & Środoń, 2009). In addition, for IAA and *MODELAGE* approaches, data points are scattered around the best fitting line (Fig. 7), which can be the result of errors in qXRD analysis. The scatter can indicate that the dated materials do not meet the assumptions behind IAA and *MODELAGE* approaches, e.g. potassium content or age value of a given polytype varies among size fractions.

Origin of the components identified in clay gouges

Compared to the surrounding rocks, the gouges are enriched in quartz and muscovite and depleted in plagioclase and K-feldspar. Unlike the High Tatra granitoids, the gouges are almost completely devoid of biotite. Other phases, which do not occur in fresh granitoids, are chlorite, calcite, $1M_d$ illite, I-S, smectite, and kaolinite. The observed differences between compositions of wallrocks and gouge follow patterns described for other shear zones developed in igneous and metamorphic rocks of similar mineralogical composition (Abad et al., 2017; Boles et al., 2018; Haines & van der Pluijm, 2012; Hayman, 2006; Surace et al., 2011).

https://doi.org/10.1007/s42860-022-00176-7 Published online by Cambridge University Press

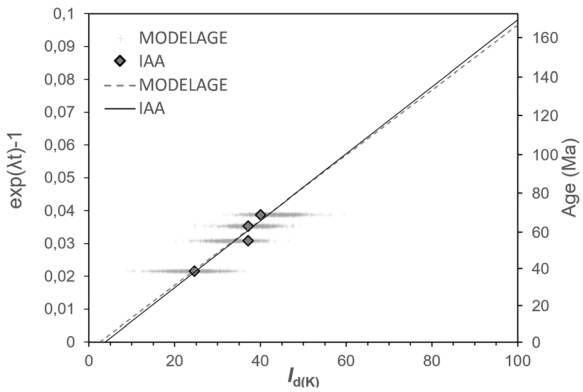

Fig. 7 Plots of $e^{\lambda t} - 1$ vs. the appropriate measure of the non-authigenic component for IAA and *MODELAGE* interpretative concepts. For *MODELAGE*, the extrapolation is for averages of 1000 runs using a Monte Carlo approach (light gray crosses). Gray diamonds and dashed extrapolation line – IAA approach.

In the investigated gouges, quartz and feldspars were inherited from the surrounding granitoids and mylonites. These minerals can be macroscopically identified in the wallrocks and as crushed grains in hand specimens of investigated samples. Larger proportions of quartz (relative to the granitoids) can be interpreted as a result of a decrease in rock volume within the shear zone (Goddard & Evans, 1995; Schleicher et al., 2009). Smectite and kaolinite are considered as authigenic components of the examined gouges. These phases do not occur in the host rocks of the gouges. A weathering origin of the smectite is considered unlikely, because it coexists with chlorite, which is broken down before precipitation of smectite during weathering (Skiba, 2007). Because the investigated materials have no signs of weathering, the small quantities of kaolinite found are also most likely authigenic. Chlorite present in studied gouges is is probably inherited from the parent rocks. Chlorite in general is commonly found in the Tatra granitoids as a product of biotite alteration (e.g. Gawęda & Włodyka, 2012; Gawęda et al., 2005; Turnau-Morawska,1948). Chloritization, which is always complete in the granitoids located next to a fault, is believed to have taken place during Alpine dynamometamorphism (Jurewicz & Bagiński, 2005; Leichmann et al., 2009), before the gouges formed.

The majority of the discrete $1M_d$ illite polytype, as well as the I-S, is authigenic and the majority of the $1M$ and $2M_1$ polytypes was inherited. During age calculations I-S was included in the $1M_d$ component and all interpretations derived for $1M_d$ illite apply also to I-S in this respect. A possible source of non-authigenic $1M_d$ polytype is wall rock containing feldspars, which often had been hydrothermally altered to sericite or illite of uncertain polytype (Uchman & Michalik, 1997). According to the best knowledge of the authors, no detailed information on sericite from the Tatra Mountains is available in the literature.

The parent rock is the most likely source of the $2M_1$ polytype, which has been considered herein as an inherited component of the gouge. Taking into account the geologic history of the area (Kohút & Sherlock, 2003; Maluski et al., 1993), the $2M_1$ polytype must have formed originally during crystallization of granitoids ~340−370 Ma, with possible recrystallization during the main Alpine event between 70 and 140 Ma.

A relatively large variability in the clay mineralogy of the gouges is exemplified by the TM4 site, where samples were taken 10–15 cm apart. This may be due to polycyclic formation of the gouges, reflecting both temporal and spatial variability of the conditions inside the gouge at the centimeter scale.

Conclusions

Clay gouges from the Tatra Mountains consist of quartz, dioctahedral mica (discrete phase, and I-S), and chlorite, commonly with plagioclase and more rarely with K-feldspar, dioctahedral smectite, calcite, or anatase. Discrete illite, mixed-layered I-S phases, chlorite, dioctahedral smectite, and kaolinite were found in fine-clay fractions (<0.2 μm) of these materials. Kaolinite and smectite are authigenic components of the clay gouges. Most if not all of the $1M_d$ polytype also belongs to this category. The rest of the phases were probably inherited from the surrounding parent rocks, but formation of $2M_1$ and $1M$ mica polytypes during one of the high-temperature stages of the shear-zone activity cannot be excluded unequivocally.

A new interpretative concept for ^{40}Ar-^{39}Ar and K-Ar dating was introduced, allowing for calculation of age values for the individual components in a three-component system. The proposed approach allows different K contents among the three components to be recognized and determined and allows compensation for the uncertainty of inherently imprecise qXRD analysis. For the investigated system, the errors associated with the results of the new interpretative concept were large, because of small differences in polytype contents among dated size fractions and, in some cases, small

https://doi.org/10.1007/s42860-022-00176-7 Published online by Cambridge University Press

relative amounts of certain polytypes. The three-component approach should be tested on samples with larger compositional variability.

Acknowledgments Artur Kuligiewicz thanks The Clay Minerals Society for supporting the research with a Student Research Grant. The fieldwork needed for the present study was conducted with the help of the Tatra National Park. Chevron ETC and Douglas McCarty are acknowledged for their permission to use their proprietary *SYBILLA* software. The authors thank Arkadiusz Derkowski for valuable discussions. Insightful comments from Joseph W. Stucki, J. M. Wampler, Austin Boles, and an anonymous reviewer greatly helped to improve the manuscript.

Availability of data and material Research Data associated with this article are stored in Mendeley Data repository and can be accessed at https://doi.org/10.17632/w4shwhhm58.1

Code availability Not applicable.

Funding This research was funded by the Student Research Grant awarded to AK by The Clay Minerals Society.

Declarations

Conflicts of interest The authors declare that they have no conflict of interest.

REFERENCES

Abad, I., Jiménez-Millán, J., Schleicher, A. M., & van der Pluijm, B. A. (2017). Mineral characterization, clay quantification and Ar-Ar dating of faulted schists in the Carboneras and Palomares Faults (Betic Cordillera, SE Spain). *European Journal of Mineralogy, 29*(1), 17–34.

Anczkiewicz, A. A., Danišik, M., & Środoń, J. (2015). Multiple low-temperature thermochronology constraints on exhumation of the Tatra Mountains: New implication for the complex evolution of the Western Carpathians in the Cenozoic. *Tectonics, 34*(11), 2296–2317.

Bense, F. A., Wemmer, K., Löbens, S., & Siegesmund, S. (2014). Fault gouge analyses: K–Ar illite dating, clay mineralogy and tectonic significance—a study from the Sierras Pampeanas, Argentina. *International Journal of Earth Sciences, 103*(1), 189–218.

Boles, A., Mulch, A., & van der Pluijm, B. (2018). Near-surface clay authigenesis in exhumed fault rock of the Alpine Fault Zone (New Zealand); O-H-Ar isotopic, XRD and chemical analysis of illite and chlorite. *Journal of Structural Geology, 111*, 27–41.

Brodie, K., Fettes, D., Harte, B., & Schmid, R. (2004). A systematic nomenclature for metamorphic rocks. 3. *Structural terms including fault-rock terms. Recommendations by the IUGS Subcommission on the systematics of metamorphic rocks. SCMR website (www. bgs. ac. uk/SCMR)*.

Burda, J., Gawęda, A., & Klötzli, U. (2011). Magma hybridization in the Western Tatra Mts. granitoid intrusion (S-Poland, Western Carpathians). *Mineralogy and Petrology, 103*, 19–36.

Burda, J., Gawęda, A., & Klötzli, U. (2013). U-Pb zircon age of the youngest magmatic activity in the High Tatra granites (Central Western Carpathians). *Geochronometria, 40*(2), 134–144.

Clauer, N. (2013). The K-Ar and $^{40}Ar/^{39}Ar$ methods revisited for dating fine-grained K-bearing clay minerals. *Chemical Geology, 354*, 163–185.

Clauer, N., Zwingmann, H., Liewig, N., & Wendling, R. (2012). Comparative $^{40}Ar/^{39}Ar$ and K–Ar dating of illite-type clay minerals: A tentative explanation for age identities and differences. *Earth-Science Reviews, 115*(1-2), 76–96.

Collins, G. (1990). *Fundamental numerical methods and data analysis*. Published by the author.

Doebelin, N., & Kleeberg, R. (2015). Profex: a graphical user interface for the Rietveld refinement program BGMN. *Journal of Applied Crystallography, 48*, 1573–1580.

Dong, H., Hall, C. M., Peacor, D. R., & Halliday, A. N. (1995). Mechanisms of argon retention in clays revealed by laser ^{40}Ar-^{40}Ar dating. *Science, 267*(5196), 355–359.

Dong, H., Hall, C. M., Halliday, A. N., Peacor, D. R., Merriman, R. J., & Roberts, B. (1997). $^{40}Ar/^{39}Ar$ illite dating of Late Caledonian (Acadian) metamorphism and cooling of K-bentonites and slates from the Welsh Basin, U.K. *Earth and Planetary Science Letters, 150*(3-4), 337–351.

Dong, H., Hall, C. M., Peacor, D. R., Halliday, A. N., & Pevear, D. R. (2000). Thermal $^{40}Ar/^{39}Ar$ separation of diagenetic from detrital illitic clays in Gulf Coast shales. *Earth and Planetary Science Letters, 175*(3-4), 309–325.

Drits, V. A., & Tchoubar, C. (1990). *X-ray diffraction by disordered lamellar structures*. Springer.

Eberl, D. D., Środoń, J., Lee, M., Nadeau, P. H., & Northorp, H. R. (1987). Sericite from the Silverton Caldera, Colorado: Correlation among structure, composition, origin, and particle thickness. *American Mineralogist, 72*, 914–934.

Fitz-Díaz, E., Hall, C. M., & van der Pluijm, B. A. (2016). XRD-based $^{40}Ar/^{39}Ar$ age correction for fine-grained illite, with application to folded carbonates in the Monterrey Salient (northern Mexico). *Geochimica et Cosmochimica Acta, 181*, 201–216.

Gawęda, A. (2007). Variscan granitoid magmatism in Tatra Mountains–the history of subduction and continental collision. *Granitoids in Poland, AM Monograph No., 1*, 319–332.

Gawęda, A., & Włodyka, R. (2012). The origin of post-magmatic Ca-Al minerals in granite-diorite mingling zones: The Tatra granitoid intrusion, Western Carpathians. *Neues Jahrbuch für Mineralogie – Abhandlungen, 190*, 29–47.

Gawęda, A., Doniecki, T., Burda, J., & Kohút, M. (2005). The petrogenesis of quartz-diorites from the Tatra Mountains (Central Western Carpathians): an example of magma hybridisation. *Neues Jahrbuch Fur Mineralogie-Abhandlungen, 181*(1), 95–109.

Gawęda, A., Szopa, K., & Chew, D. (2014). LA-ICP-MS U-Pb dating and REE patterns of apatite from the Tatra Mountains, Poland as a monitor of the regional tectonomagmatic activity. *Geochronometria, 41*(4), 304–314.

Goddard, J. V., & Evans, J. P. (1995). Chemical-changes and fluid-rock interaction in faults of crystalline thrust sheets, northwestern Wyoming, USA. *Journal of Structural Geology, 17*(4), 533–547.

Grathoff, G. H., & Moore, D. M. (1996). Illite polytype quantification using WILDFIRE© calculated X-ray diffraction patterns. *Clays and Clay Minerals, 44*(6), 835–842.

Haines, S. H., & van der Pluijm, B. A. (2008). Clay quantification and Ar-Ar dating of synthetic and natural gouge: Application to the Miocene Sierra Mazatan detachment fault, Sonora, Mexico. *Journal of Structural Geology, 30*(4), 525–538.

Haines, S. H., & van der Pluijm, B. A. (2012). Patterns of mineral transformations in clay gouge, with examples from low-angle normal fault rocks in the western USA. *Journal of Structural Geology, 43*, 2–32.

Hall, C. M. (2014). Direct measurement of recoil effects on $^{40}Ar/^{39}Ar$ standards. In F. Jourdan, D. F. Mark, & C. Verati (eds), Advances in $^{40}Ar/^{39}Ar$ Dating: From Archaeology to Planetary Sciences (pp. 53–62). Geological Society Special Publications 378(1), Geological Society, London.

Hayman, N. W. (2006). Shallow crustal fault rocks from the Black Mountain detachments, Death Valley, CA. *Journal of Structural Geology, 28*(10), 1767–1784.

Jackson, M. L. (1969). Soil Chemical Analysis-Advanced Course. Madison, WI: published by the author.

Jurewicz, E. (2005). Geodynamic evolution of the Tatra Mts. and the Pieniny Klippen Belt (Western Carpathians): problems and comments. *Acta Geologica Polonica, 55*(3), 295–338.

Jurewicz, E. (2006). Petrophysical control on the mode of shaering in the sedimentary rocks and granitoid core of the Tatra Mountains during Late Cretaceous nappe-thrusting and folding, Carpathians, Poland. *Acta Geologica Polonica, 56*(2), 159–170.

Jurewicz, E., & Bagiński, B. (2005). Deformation phases in the selected shear zones within the Tatra Mountains granitoid core. *Geologica Carpathica, 56*, 17–28.

Jurewicz, E., & Kozłowski, A. (2003). Formation conditions of quartz mineralization in the mylonitic zones and on the slickenside fault planes in the High Tatra granitoids. *Archiwum Mineralogiczne, 54*, 65–76.

Kelley, S. (2002). K-Ar and Ar-Ar dating. *Reviews in Mineralogy and Geochemistry, 47*(1), 785–818.

Kohút, M., & Sherlock, S. C. (2003). Laser microprobe ^{40}Ar-^{39}Ar analysis of pseudotachylyte and host-rocks from the Tatra Mountains, Slovakia: evidence for late Palaeogene seismic/tectonic activity. *Terra Nova, 15*(6), 417–424.

Králiková, S., Vojtko, R., Sliva, U., Minár, J., Fügenschuh, B., Kováč, M., & Hók, J. (2014). Cretaceous—Quaternary tectonic evolution of the Tatra Mts (Western Carpathians): constraints from structural, sedimentary, geomorphological, and fission track data. *Geologica Carpathica, 65*(4), 307–326.

Kuligiewicz, A., Derkowski, A., Szczerba, M., Gionis, V., & Chryssikos, G. D. (2015). Revisiting the infrared spectrum of the water–smectite interface. *Clays and Clay Minerals, 63*(1), 15–29.

Leichmann, J., Jacher-Sliwczynska, K., & Broska, I. (2009). Element mobility and fluid path ways during feldspar alteration: textural evidence from cathodoluminescece and electron microprobe study of an example from tonalites (High Tatra, Poland-Slowakia). *Neues Jahrbuch für Mineralogie – Abhandlungen, 186*, 1–10.

Maluski, H., Rajlich, P., & Matte, P. (1993). ^{40}Ar-^{39}Ar dating of the Inner Carpathians Variscan basement and Alpine mylonitic overprinting. *Tectonophysics, 223*(3-4), 313–337.

Mancktelow, N., Zwingmann, H., & Mulch, A. (2016). Timing and conditions of clay fault gouge formation on the Naxos detachment (Cyclades, Greece). *Tectonics, 35*(10), 2334–2344.

McCarty, D. K., Sakharov, B. A., & Drits, V. A. (2009). New insights into smectite illitization: A zoned K-bentonite revisited. *American Mineralogist, 94*(11-12), 1653–1671.

Moore, D., & Reynolds, R. (1997). *X-ray Diffraction and the Identification and Analysis of Clay Minerals*. Oxford University Press.

Peacor, D. R., Bauluz, B., Dong, H., Tillick, D., & Yonghong, Y. (2002). Transmission and analytical electron microscopy evidence for high Mg contents of 1*M* illite: absence of 1*M* polytypism in normal prograde diagenetic sequences of pelitic rocks. *Clays and Clay Minerals, 50*(6), 757–765.

Pevear, D. R. (1992). Illite age analysis, a new tool for basin thermal history analysis. In Y. K. Kharaka & A. S. Maest (Eds.), *Water-rock interaction* (pp. 1251–1254). AA Balkema.

Pevear, D. R. (1999). Illite and hydrocarbon exploration. *Proceedings of the National Academy of Sciences, 96*, 3440–3446.

Piotrowska, K. (1970). Fotointerpretacja i geneza struktur nieciągłych w polskiej części Tatr Wysokich. *Acta Geologica Polonica, 20*, 365–411 [in Polish].

Plašienka, D., Grecula, P., Putiš, M., Kováč, M., & Hovorka, D. (1997). Evolution and structure of the Western Carpathians: an overview. In P. Grecula, D. Hovorka, & M. Putiš (Eds.), *Geological evolution of the Western Carpathians* (pp. 1–24). Mineralia Slovaca – Monograph.

Russell, J. D., & Farmer, V. C. (1964). Infra-red spectroscopic study of the dehydration of montmorillonite and saponite. *Clay Minerals Bulletin, 5*(32), 443–464.

Samson, S. D., & Alexander, E. C. (1987). Calibration of the interlaboratory ^{40}Ar-^{39}Ar dating standard, MMhb-1. *Chemical Geology: Isotope Geoscience section, 66*(1), 27–34.

Schleicher, A. M., Warr, L. N., & van der Pluijm, B. (2009). On the origin of mixed-layered clay minerals from the San Andreas Fault at 2.5-3 km vertical depth (SAFOD drillhole at Parkfield, California). *Contributions to Mineralogy and Petrology, 157*(2), 173–187.

Sibson, R. (1977). Fault rocks and fault mechanisms. *Journal of the Geological Society, 133*(3), 191–213.

Skiba, M. (2007). Clay mineral formation during podzolization in an alpine environment of the Tatra Mountains, Poland. *Clays and Clay Minerals, 55*(6), 618–634.

Śmigielski, M., Sinclair, H. D., Stuart, F. M., Persano, C., & Krzywiec, P. (2016). Exhumation history of the Tatry Mountains, Western Carpathians, constrained by low-temperature thermochronology. *Tectonics, 35*(1), 187–207.

Solum, J. G., van der Pluijm, B. A., & Peacor, D. R. (2005). Neocrystallization, fabrics and age of clay minerals from an exposure of the Moab Fault, Utah. *Journal of Structural Geology, 27*(9), 1563–1576.

Środoń, J. (1999). Use of clay minerals in reconstructing geological processes: recent advances and some perspectives. *Clay Minerals, 34*(1), 27–37.

Środoń, J. (2013). Identification and Quantitative Analysis of Clay Minerals. In F. Bergaya, & G. Lagaly (eds), Handbook of Clay Science (pp. 25–49). Developments in Clay Science 5, Elsevier, Amsterdam.

Środoń, J., Zeelmaekers, E., & Derkowski, A. (2009). The charge of component layers of illite-smectite in bentonites and the nature of end-member illite. *Clays and Clay Minerals, 57*(5), 649–671.

Steiger, R. H., & Jäger, E. (1977). Subcommission on geochronology: Convention on use of decay constants in geo- and cosmochronology. *Earth and Planetary Science Letters, 36*(3), 359–362.

Surace, I. R., Clauer, N., Thélin, P., & Pfeifer, H.-R. (2011). Structural analysis, clay mineralogy and K-Ar dating of fault gouges from Centovalli Line (Central Alps) for reconstruction of their recent activity. *Tectonophysics, 510*(1-2), 80–93.

Szczerba, M., & Środoń, J. (2009). Extraction of diagenetic and detrital ages and of the $^{40}K_{detrital}/^{40}K_{diagenetic}$ ratio from K-Ar dates of clay fractions. *Clays and Clay Minerals, 57*(1), 93–103.

Torgersen, E., Viola, G., Zwingmann, H., & Harris, C. (2014). Structural and temporal evolution of a reactivated brittle-ductile fault - Part II: Timing of fault initiation and reactivation by K-Ar dating of synkinematic illite/muscovite. *Earth and Planetary Science Letters, 407*, 221–233.

Turnau-Morawska, M. (1948). Z mikrogeologii trzonu krystalicznego Tatr (Microgeological researches in central part of the crystaline Tatra). *Kosmos seria A*, 65, 59-100. In Polish with English summary.

Uchman, A. & Michalik, M. (1997) Podłoże geologiczne In: Plan Ochrony TPN. Operat ochrona przyrody nieożywionej i gleb. S. Skiba, A. Kotarba (Ed.). Zakopane: Tatrzański Park Narodowy [in Polish]

Ufer, K., Kleeberg, R., Bergmann, J., & Dohrmann, R. (2012). Rietveld refinement of disordered illite-smectite mixed-layer structures by a recursive algorithm. I: One-dimensional patterns. *Clays and Clay Minerals, 60*(5), 507–534.

van der Pluijm, B., & Hall, C. M. (2015). Fault Zone (Thermochronology). In W. Jack Rink & J. W. Thompson (Eds.), *Encyclopedia of Scientific Dating Methods* (pp. 269–274). Springer Netherlands.

van der Pluijm, B. A., Hall, C. M., Vrolijk, P. J., Pevear, D. R., & Covey, M. C. (2001). The dating of shallow faults in the Earth's crust. *Nature, 412*(6843), 172–175.

Viola, G., Zwingmann, H., Mattila, J., & Kapyaho, A. (2013). K-Ar illite age constraints on the Proterozoic formation and reactivation history of a brittle fault in Fennoscandia. *Terra Nova, 25*(3), 236–244.

Yan, Y., Tillick, D., Peacor, D. R., & Simmons, S. F. (2001). Genesis of dioctahedral phyllosilicates during hydrothermal alteration of volcanic rocks: II The Broadlands-Ohaaki hydrothermal system, New Zealand. *Clays and Clay Minerals, 49*(2), 141–155.

Ylagan, R. F., Pevear, D. R., & Vrolijk, P. J. (2000). Discussion of "Extracting K-Ar ages from shales: a theoretical test". *Clay Minerals, 35*(3), 599–604.

Ylagan, R. F., Kim, C. S., Pevear, D. R., & Vrolijk, P. J. (2002). Illite polytype quantification for accurate K-Ar age determination. *American Mineralogist, 87*(11-12), 1536–1545.

York, D., Evensen, N. M., Lopez Martinez, M., & De Basabe Delgado, J. (2004). Unified equations for the slope, intercept, and standard errors of the best straight line. *American Journal of Physics, 72*(3), 367–375.

https://doi.org/10.1007/s42860-022-00176-7 Published online by Cambridge University Press